

CHALMERS
UNIVERSITY OF TECHNOLOGY

Comparison of Macro-Basis-Function Construction Methods for Reduced-Order Analysis of Cavity-Backed Reflectarrays

Downloaded from: https://research.chalmers.se, 2026-11-22 16:55 UTC

Citation for the original published paper (version of record):
Lin, D., Manholm, L., Talcoth, O. et al (2026). Comparison of Macro-Basis-Function Construction Methods for Reduced-Order Analysis of
Cavity-Backed Reflectarrays. Proceedings of the International Conference on Electromagnetics in Advanced Applications, ICEAA(2026): 584-589.
http://dx.doi.org/10.23919/ICEAA69870.2026.11724733

N.B. When citing this work, cite the original published paper.

© 2026 IEEE. Personal use of this material is permitted. Permission from IEEE must be obtained for all other uses, in any current or future media, including reprinting/republishing this material for advertising or promotional purposes, or reuse of any copyrighted component of this work in other works.

(article starts on next page)

Comparison of Macro-Basis-Function Construction Methods for Reduced-Order Analysis of Cavity-Backed Reflectarrays

Dijun Lin*†, Lars Manholm†, Oskar Talcoth†, and Rob Maaskant*
*Antenna Group, Department of Electrical Engineering, Chalmers University of Technology, Gothenburg, Sweden
{dijun, rob.maaskant}@chalmers.se
†Ericsson Research, Gothenburg, Sweden
{dijun.lin, lars.manholm, oskar.talcoth}@ericsson.com

***Abstract*—This letter presents a controlled comparison of three macro-basis-function (MBF) constructions for reduced-order method-of-moments analysis of cavity-backed reflectarrays: characteristic mode analysis (CMA), the characteristic basis function method with primary and enriched responses (CBFM), and a singular-value-decomposition (SVD)-based basis. The comparison is performed within a common reduced-order formulation using identical geometry, discretization, partitioning, and solver settings, so that differences in current reconstruction, far-field accuracy, compression, and conditioning can be attributed mainly to the MBF construction. A single element and an identical-element 8x8 array are used as benchmarks at 32 GHz. The results show that CBFM provides attractive low-rank accuracy but exhibits nonmonotonic solution error as enriched functions are retained. Explicit G-orthogonalization substantially improves the conditioning and accuracy of CMA, whereas the SVD basis gives the best-conditioned reduced systems but requires more MBFs to reach the prescribed far-field accuracy. The array results preserve the main single-element current-reconstruction and conditioning trends, while the far-field error is less sensitive to the retained basis size.**

***Index Terms*—Cavity-backed reflectarrays, characteristic basis function method, characteristic mode analysis, macro-basis functions, method of moments, reduced-order modeling.**

I. Introduction

Large-scale reflectarray simulations based on the method of moments (MoM) often lead to dense or ill-conditioned linear systems, resulting in substantial computational cost, especially when repeated solutions are required for multiple excitations or parameter sweeps. Macro-basis functions (MBFs) reduce the number of unknowns by constructing a low-dimensional subspace that captures the dominant current or field behavior, thereby accelerating the solution while maintaining good accuracy [1], [2].

This paper extends the cavity-backed reflectarray framework introduced in [3]–[7] by isolating the effect of MBF construction within that formulation. Whereas the earlier work established the underlying MFIE–PO framework and used MBFs as an enabling ingredient, it did not examine in a controlled manner how the basis-construction strategy itself affects compression, conditioning, and field accuracy. The present paper therefore provides a controlled comparison of characteristic mode analysis (CMA) [8]–[13], the characteristic basis function method (CBFM) [14]–[23], and singular value decomposition (SVD), with multi-order CBF enrichment treated within the CBFM framework [24]–[26].

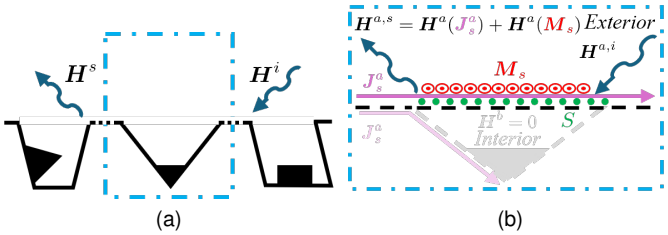


Fig. 1. Formulation steps for a cavity-backed reflectarray. (a) Original scattering problem with incident and scattered magnetic fields, $\boldsymbol{H}^i$ and $\boldsymbol{H}^s$. (b) Application of the equivalence principle on S, introducing the equivalent magnetic current $\boldsymbol{M}_s$ and suppressing the fields in region b. The reduced problem is then obtained by neglecting rear-surface currents, so that the three-dimensional conductor is replaced by a two-dimensional PEC sheet in the aperture plane.

This letter presents a controlled benchmark of CMA-, CBFM-, and SVD-based MBF constructions for cavity-backed reflectarray analysis, isolating the effect of the basis construction by keeping the geometry, discretization, partitioning, and reduced-order solver fixed. The considered approaches are evaluated in terms of reconstructed-current accuracy, far-field accuracy, compression efficiency, and numerical stability through the condition number of the reduced system. In addition, the study examines how closely single-element behavior predicts finite-array performance. The main contributions are a unified reduced-order framework for CMA-, CBFM-, and SVD-based MBFs, a controlled benchmark of their accuracy-versus-rank and conditioning behavior, and an assessment of how single-element trends carry over to the array case.

The remainder of this paper is organized as follows. Section II briefly summarizes the underlying formulation and introduces the considered MBF constructions. Section III presents the numerical results. Finally, Section IV concludes the paper.

II. Macro-Basis Functions and System Compression

A. MFIE–PO Formulation

The underlying cavity-backed reflectarray formulation follows [3]–[7] and is briefly summarized here for completeness.

The scattering problem is decomposed into exterior and interior domains separated by the aperture surface S, as illustrated in Fig. 1a. Applying the equivalence principle on S introduces the equivalent magnetic current $\boldsymbol{M}_s$ and suppresses the fields in the interior region, leading to the reduced problem shown in Fig. 1b. Enforcing tangential magnetic-field continuity on S yields the MFIE on the aperture [6], [27], [28]:

$$\big[\boldsymbol{H}^a(\boldsymbol{M}_s) + \boldsymbol{H}^b(\boldsymbol{M}_s)\big]_{\tan} + \big[\boldsymbol{H}^a(\boldsymbol{J}_s^a) - \boldsymbol{H}^b(\boldsymbol{J}_s^b)\big]_{\tan} = \big[\boldsymbol{H}^{b,i} - \boldsymbol{H}^{a,i}\big]_{\tan}. \quad (1)$$

Here, $\boldsymbol{M}_s$ denotes the equivalent aperture magnetic current, while $\boldsymbol{J}_s^a$ and $\boldsymbol{J}_s^b$ denote the equivalent electric currents on the exterior and interior sides of the aperture, respectively. The operators $\boldsymbol{H}^a(\cdot)$ and $\boldsymbol{H}^b(\cdot)$ denote the corresponding magnetic-field integral operators.

For the reduced problem in Fig. 1b, the MFIE is combined with the proposed PO boundary condition [7] and discretized using Galerkin testing with Rao-Wilton-Glisson (RWG) basis functions [29]. With the testing inner product $\langle \mathbf{a}, \mathbf{b} \rangle = \int_S \mathbf{a} \cdot \mathbf{b}\, \mathrm{d}S$, the resulting system becomes [7]

$$\big[\mathbf{Y}_{\mathrm{tot}}^a + \mathbf{Y}_{\mathrm{tot}}^b\big]\,\mathbf{V} = \mathbf{I}, \quad (2a)$$

$$\big[\mathbf{Y}_{\mathrm{tot}}^a\big]_{mn} = 2\,\big\langle \boldsymbol{f}_m^M, \boldsymbol{H}^a(\boldsymbol{f}_n^M)\big\rangle, \quad (2b)$$

$$\big[\mathbf{I}\big]_m = -2\,\big\langle \boldsymbol{f}_m^M, \boldsymbol{H}^{a,i}\big\rangle, \quad (2c)$$

$$\big[\mathbf{Y}_{\mathrm{tot}}^b\big]_{mn} = \big\langle \boldsymbol{f}_m^M, \boldsymbol{H}^b(\boldsymbol{f}_n^M)\big\rangle - \big\langle \boldsymbol{f}_m^M, \boldsymbol{H}^b\Big(\boldsymbol{J}_s^b(-\boldsymbol{f}_n^M)\Big)\big\rangle. \quad (2d)$$

Here, $\boldsymbol{f}_m^M$ denotes the RWG basis/testing function with local support on S associated with the aperture magnetic current, $\mathbf{V} \in \mathbb{C}^{N\times 1}$ collects the unknown coefficients, $\mathbf{Y}_{\mathrm{tot}}^a$ is the dense exterior-domain matrix, and $\mathbf{Y}_{\mathrm{tot}}^b$ is the cavity-admittance matrix associated with the interior domain.

For an array of L elements drawn from P unique element types, the interior matrix is block diagonal,

$$\mathbf{Y}_{\mathrm{tot}}^b = \mathrm{blkdiag}\big(\mathbf{Y}^{b,(\tau(1))}, \ldots, \mathbf{Y}^{b,(\tau(L))}\big), \quad (3)$$

where $\tau(l) \in \{1, \ldots, P\}$ denotes the type index of element l. Thus, each unique element type is characterized only once and reused throughout the array [3].

B. MBF Compression

The problem is well suited for MBF compression because the apertures of different elements are physically separated, allowing an element-wise reduced basis with nonoverlapping supports. Let $\mathbf{V}_{\mathrm{MBF}} \in \mathbb{C}^{N\times K}$ denote the MBF matrix, whose columns contain the MBFs expressed in the original RWG basis, and let $\mathbf{w} \in \mathbb{C}^K$ collect the corresponding MBF weights. The aperture current is expanded as

$$\mathbf{V} = \mathbf{V}_{\mathrm{MBF}}\mathbf{w}. \quad (4)$$

If K_l MBFs are retained for element l, the total number of MBFs is $K = \sum_{l=1}^{L} K_l$, and the global basis matrix is assembled as

$$\mathbf{V}_{\mathrm{MBF}} = \mathrm{blkdiag}\big(\mathbf{V}_{\mathrm{MBF}}^{(\tau(1))}, \ldots, \mathbf{V}_{\mathrm{MBF}}^{(\tau(L))}\big). \quad (5)$$

With $\mathbf{Y} = \mathbf{Y}_{\mathrm{tot}}^a + \mathbf{Y}_{\mathrm{tot}}^b$, substitution of (4) into (2a) and multiplying by $\mathbf{V}_{\mathrm{MBF}}^{\mathrm{T}}$, yields

$$\widetilde{\mathbf{Y}}\mathbf{w} = \widetilde{\mathbf{I}}, \quad (6)$$

where

$$\widetilde{\mathbf{Y}} = \mathbf{V}_{\mathrm{MBF}}^{\mathrm{T}}\mathbf{Y}\mathbf{V}_{\mathrm{MBF}}, \qquad \widetilde{\mathbf{I}} = \mathbf{V}_{\mathrm{MBF}}^{\mathrm{T}}\mathbf{I}.$$

Because the same nonconjugated testing product $\langle \cdot, \cdot \rangle$ is used in the projection, the superscript T denotes transpose rather than Hermitian transpose. After solving for $\mathbf{w}$, the full-resolution current follows from (4). All methods considered here use the same reduced formulation and differ only in the construction and ordering of the columns of $\mathbf{V}_{\mathrm{MBF}}$.

MBFs may be excitation-dependent or excitation-independent. Excitation-dependent MBFs are often more efficient but may be biased toward the used excitation set, whereas excitation-independent MBFs may generalize better across excitations. In the present comparison, CBFM is an excitation-dependent construction, whereas CMA and the system matrix-based SVD (called SVD hereafter) are excitation-independent.

C. Compression and Conditioning

To assess the numerical robustness of the compressed MBF representation, the spectral condition number of the reduced matrix $\widetilde{\mathbf{Y}}$ is monitored [30], [31]:

$$\kappa_2(\widetilde{\mathbf{Y}}) = \|\widetilde{\mathbf{Y}}\|_2\,\|\widetilde{\mathbf{Y}}^{-1}\|_2 = \frac{\sigma_{\max}(\widetilde{\mathbf{Y}})}{\sigma_{\min}(\widetilde{\mathbf{Y}})}, \quad (7)$$

where $\sigma_{\max}(\cdot)$ and $\sigma_{\min}(\cdot)$ denote the largest and smallest singular values, respectively.

To separate self-interaction from inter-element coupling, the reduced matrix is written as

$$\widetilde{\mathbf{Y}} = \mathbf{D} + \mathbf{C}, \qquad \mathbf{D} = \mathrm{blkdiag}\big(\widetilde{\mathbf{Y}}_{11}, \ldots, \widetilde{\mathbf{Y}}_{LL}\big), \quad (8)$$

where $\mathbf{D}$ contains the block-diagonal self-interaction terms and $\mathbf{C}$ contains the off-diagonal coupling blocks. If $\mathbf{D}$ is nonsingular, then

$$\widetilde{\mathbf{Y}} = \mathbf{D}\big(\mathbf{I} + \mathbf{D}^{-1}\mathbf{C}\big), \quad (9)$$

and therefore

$$\kappa_2(\widetilde{\mathbf{Y}}) \le \kappa_2(\mathbf{D})\,\kappa_2\big(\mathbf{I} + \mathbf{D}^{-1}\mathbf{C}\big). \quad (10)$$

Thus, the conditioning of the full reduced system depends on both the conditioning of the local reduced blocks and the strength of the inter-element coupling represented by $\mathbf{D}^{-1}\mathbf{C}$. For weak coupling, the conditioning of the local reduced blocks can therefore provide a useful a priori indicator of the array-level conditioning.

A large condition number indicates increased sensitivity to numerical perturbations and may also degrade the convergence behavior of iterative solvers, although it does not by itself determine the final solution accuracy. The practical basis size is therefore governed by a tradeoff between approximation accuracy and numerical robustness, since adding more MBFs may eventually increase sensitivity more than it improves the approximation.

D. MBF Types Considered

Three MBF construction strategies are considered: characteristic mode analysis (CMA), the characteristic basis function method (CBFM), and an SVD-based construction. For each unique element type p, a local basis matrix $\mathbf{V}_{\mathrm{MBF}}^{(p)}$ is constructed from the corresponding isolated-element matrix and mapped to all array elements of the same type through the global assembly described above.

Each construction is used with its natural normalization or truncation procedure. Thus, the comparison evaluates the reduced bases as generated by each method, rather than enforcing a common Euclidean normalization. A purely Euclidean normalization of the CMA modes would define a modified CMA basis and is not considered here.

1) Characteristic-Mode-Based MBFs: CMA provides an excitation-independent MBF construction in which the basis functions are derived from the intrinsic current modes of each element geometry. For each unique element type p, let

$$\mathbf{Y}^{(p)} = \mathbf{G}^{(p)} + j\mathbf{B}^{(p)}, \tag{11}$$

with

$$\mathbf{G}^{(p)} = \tfrac{1}{2}\left(\mathbf{Y}^{(p)} + \mathbf{Y}^{(p)\mathrm{H}}\right), \qquad \mathbf{B}^{(p)} = \tfrac{1}{2j}\left(\mathbf{Y}^{(p)} - \mathbf{Y}^{(p)\mathrm{H}}\right).$$

In the admittance-based formulation adopted here, the characteristic currents are obtained from [12]

$$\mathbf{B}^{(p)}\mathbf{v}_n^{(p)} = \lambda_n^{(p)}\,\mathbf{G}^{(p)}\mathbf{v}_n^{(p)}, \tag{12}$$

where $\lambda_n^{(p)}$ and $\mathbf{v}_n^{(p)}$ denote the characteristic value and eigenvector of mode n, respectively. The corresponding modal significance is

$$\mathrm{MS}_n^{(p)} = \frac{1}{\sqrt{1+\left(\lambda_n^{(p)}\right)^2}}. \tag{13}$$

The modes with the largest modal significance values are retained as MBFs. Let

$$\mathbf{V}_{\mathrm{raw}}^{(p)} = \left[\mathbf{v}_{n_1}^{(p)}, \mathbf{v}_{n_2}^{(p)}, \ldots, \mathbf{v}_{n_{m_p}}^{(p)}\right] \tag{14}$$

denote the matrix of selected raw characteristic eigenvectors, where m_p is the number of retained modes for element type p.

To improve numerical robustness, the selected raw characteristic modes are normalized and re-orthogonalized in the G-metric. Define

$$\mathbf{S}^{(p)} = \mathbf{V}_{\mathrm{raw}}^{(p)\mathrm{H}}\mathbf{G}^{(p)}\mathbf{V}_{\mathrm{raw}}^{(p)}, \tag{15}$$

with eigendecomposition

$$\mathbf{S}^{(p)} = \mathbf{Q}^{(p)}\mathbf{D}_g^{(p)}\mathbf{Q}^{(p)\mathrm{H}}. \tag{16}$$

Here, $\mathbf{Q}^{(p)}$ contains the eigenvectors of $\mathbf{S}^{(p)}$ and $\mathbf{D}_g^{(p)}$ its eigenvalues. Since these eigenvalues may be negative or very small, the local CMA basis is formed as

$$\mathbf{V}_{\mathrm{CMA}}^{(p)} = \mathbf{V}_{\mathrm{raw}}^{(p)}\mathbf{Q}^{(p)}\left|\mathbf{D}_g^{(p)}\right|^{-1/2}, \tag{17}$$

where very small eigenvalue magnitudes may be thresholded in practice. This step compensates for numerical scaling and loss of orthogonality, yielding a G-orthogonalized basis. If the raw characteristic modes are already strictly G-orthogonal, then $\mathbf{S}^{(p)}$ is diagonal and the procedure reduces to G-metric normalization.

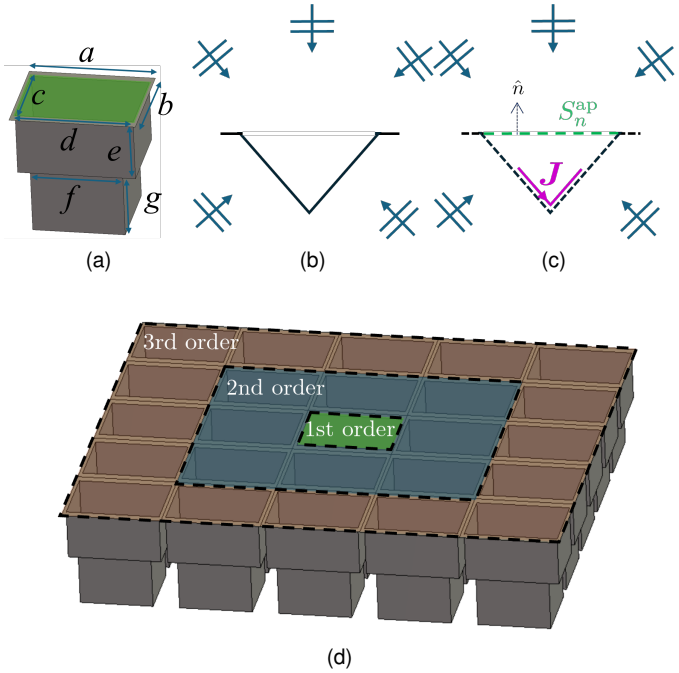


Fig. 2. Construction of the CBF basis. (a) Unit-cell geometry with $a = 6$ mm, $b = 5.6$ mm, $c = 5$ mm, $d = 4$ mm, $e = 3$ mm, $f = 4.4$ mm, and $g = 3$ mm. (b) Schematic illustration of the simplified model used for primary CBF generation under plane-wave excitation. (c) Schematic illustration of the corresponding aperture field at S_n^{ap} obtained from the equivalent-current formulation under plane-wave illumination. (d) Local-subarray enrichment used to capture higher-order coupling effects.

The main advantage of CMA is that it provides a physically interpretable and excitation-independent reduced space. However, because the basis is not tailored to a particular excitation set, additional modes may be required to capture excitation-specific current features.

2) CBFM-Based MBFs: CBFM constructs excitation-dependent MBFs from current responses to a prescribed set of excitations [16], [17], [20]–[23]. For each element type p, the primary CBFs are generated by illuminating an isolated element with a representative set of plane waves, as illustrated in Fig. 2b, and solving

$$\mathbf{Z}^{(p)}\mathbf{I}^{(p)} = \mathbf{v}^{(p)}, \tag{18}$$

where $\mathbf{Z}^{(p)}$ denotes the local impedance matrix, $\mathbf{I}^{(p)}$ the induced current vector, and $\mathbf{v}^{(p)}$ the excitation vector.

The induced currents are then used to extract the electric field at the aperture of the central element, as illustrated in Fig. 2c. The equivalent aperture magnetic current is then obtained as $\mathbf{M}_s = \mathbf{E}\times\hat{\mathbf{n}}$ [32], where $\hat{\mathbf{n}}$ denotes the outward unit vector, normal to the aperture. The resulting aperture responses define the primary CBFs used in the reduced formulation.

To enrich the basis, the same procedure is repeated for local subarrays centered on the considered element. In this work, 3×3 and 5×5 subarrays are used to generate additional responses that capture secondary and tertiary coupling effects,

as illustrated in Fig. 2d. The primary and enrichment responses are collected into a response matrix $\mathbf{R}^{(p)} = [\mathbf{r}_1^{(p)}, \ldots, \mathbf{r}_{q_p}^{(p)}]$, where q_p is the total number of responses for element type p. An SVD-based truncation,

$$\mathbf{R}^{(p)} = \mathbf{U}_R^{(p)} \mathbf{\Sigma}_R^{(p)} \mathbf{W}_R^{(p)\mathrm{H}}, \tag{19}$$

is then applied to retain only the dominant left singular vectors. The local CBFM basis is therefore

$$\mathbf{V}_{\mathrm{CBFM}}^{(p)} = \mathbf{U}_R^{(p)}(:, 1\!:\!m_p) = \left[\mathbf{b}_1^{(p)}, \mathbf{b}_2^{(p)}, \ldots, \mathbf{b}_{m_p}^{(p)}\right], \tag{20}$$

where $\mathbf{b}_k^{(p)}$ denotes the k-th retained basis function for element type p.

Thus, isolated-element responses define the primary CBFs, whereas subarray responses provide enrichment functions. The SVD step removes redundancy and controls the basis size, improving compactness at additional offline cost. CBFM provides efficient compression when the selected excitations are representative of the operating conditions; however, its performance may degrade for unseen excitation scenarios. For arrays with multiple element types, the enrichment procedure also becomes increasingly expensive because the number of possible local environment configurations grows combinatorially. In the worst case, for P distinct element types and a local environment containing n elements, the number of type combinations scales as P^n. Consequently, the array-level CBFM results reported in Section III are restricted to the identical-element benchmark.

3) SVD-Based MBFs: In the SVD-based approach, the MBFs are constructed directly from the inverse local system operator rather than from selected excitation responses, as in CBFM. For each unique element type p, let

$$\mathbf{Y}^{(p)} = \mathbf{U}^{(p)} \mathbf{\Sigma}^{(p)} \mathbf{W}^{(p)\mathrm{H}} \tag{21}$$

be the singular value decomposition of the local system matrix. Then

$$\left(\mathbf{Y}^{(p)}\right)^{-1} = \mathbf{W}^{(p)} \left(\mathbf{\Sigma}^{(p)}\right)^{-1} \mathbf{U}^{(p)\mathrm{H}}, \tag{22}$$

so that the dominant left singular vectors of $\left(\mathbf{Y}^{(p)}\right)^{-1}$ are the right singular vectors of $\mathbf{Y}^{(p)}$ associated with its smallest singular values. If N_p denotes the number of local aperture unknowns and $\mathbf{w}_k^{(p)}$ the k-th column of $\mathbf{W}^{(p)}$, the local SVD basis is

$$\mathbf{V}_{\mathrm{SVD}}^{(p)} = \left[\mathbf{w}_{N_p - m_p + 1}^{(p)}, \ldots, \mathbf{w}_{N_p}^{(p)}\right]. \tag{23}$$

This yields an excitation-independent algebraic reduced basis. However, unlike CBFM, it is not tailored to a particular excitation class and does not in general admit a direct physical interpretation.

E. Error Metrics

The following error metrics are reported as functions of the basis size m or the compression ratio m/N:

- Relative current reconstruction error:

$$\varepsilon_{\mathrm{rel}} = \frac{\|\mathbf{V}_{\mathrm{MBF}}\mathbf{w} - \mathbf{V}\|_2}{\|\mathbf{V}\|_2}. \tag{24}$$

TABLE I
CBFM BASIS-GENERATION SETTINGS FOR PRIMARY AND ENRICHED CBFS. BOTH θ- AND ϕ-POLARIZED PLANE-WAVE EXCITATIONS ARE INCLUDED FOR EACH SAMPLED DIRECTION.

CBF Type	Responses	Time	θ Step	ϕ Step
Primary CBF	180	0.6 s	20°	45°
Secondary CBF	180	4 s	20°	45°
Tertiary CBF	180	42 s	20°	45°

TABLE II
MINIMUM NUMBER OF RETAINED MBFS PER ELEMENT AND CORRESPONDING REDUCED DIMENSION K REQUIRED TO REACH AN ARRAY-LEVEL FAR-FIELD ERROR BELOW 10^{-3}. THE FULL-ORDER ARRAY SYSTEM CONTAINS $64 \times 330 = 21120$ UNKNOWNS.

Method	Retained MBFs	K	$\bar{e}$	$\varepsilon_{\mathrm{rel}}$	κ_2
CMA	8	512	0.79×10^{-3}	0.86	116
$\mathrm{CMA}_{\mathrm{G\text{-}orth}}$	8	512	0.79×10^{-3}	0.15	116
CBFM	120	7680	0.98×10^{-3}	0.26	358
SVD	253	16192	0.96×10^{-3}	0.01	157

- Peak-normalized mean radiation-pattern error, computed over all sampled angular points of the full radiation pattern using the sampled pattern values x_i in linear scale:

$$e_i = \frac{\left|x_i^{\mathrm{ref}} - x_i\right|}{\max_j \left|x_j^{\mathrm{ref}}\right|}, \qquad \bar{e} = \frac{1}{N_\Omega} \sum_{i=1}^{N_\Omega} e_i, \tag{25}$$

  where N_Ω denotes the total number of sampled angular points. This normalization avoids disproportionately large relative errors near deep pattern nulls.

Together, these metrics provide a consistent basis for comparing the considered MBF constructions in terms of current reconstruction and radiation-pattern accuracy.

III. RESULTS

The different MBF constructions are evaluated for both a single element and an identical-element 8×8 array under identical formulation, discretization, and solver settings. Validation uses a horn illumination located approximately 10.7λ above the array center. The unit-cell geometry is shown in Fig. 2a, and the full-order RWG solution is used as the reference. The operating frequency is 32 GHz, matching the benchmark in [7].

For CBFM, Table I summarizes the number of generated candidate responses, generation time, and angular sampling of the plane-wave excitation set. Both θ- and ϕ-polarized incident plane waves are included for each sampled direction. The reported CBFM results use combined primary and enriched CBFs. At the array level, enrichment is restricted to identical-element arrays, since nonidentical local environments become computationally prohibitive. For the present single-type benchmark, the CMA- and SVD-based bases are generated from the isolated-element matrix, whereas CBFM requires separate response simulations for the plane-wave excitation set and enrichment configurations.

Figures 3a and 3b show the full-range single-element and 8×8 array results, respectively. The single-element results include relative current reconstruction error and the local reduced-block condition number $\kappa_2(\mathbf{D})$, whereas the array

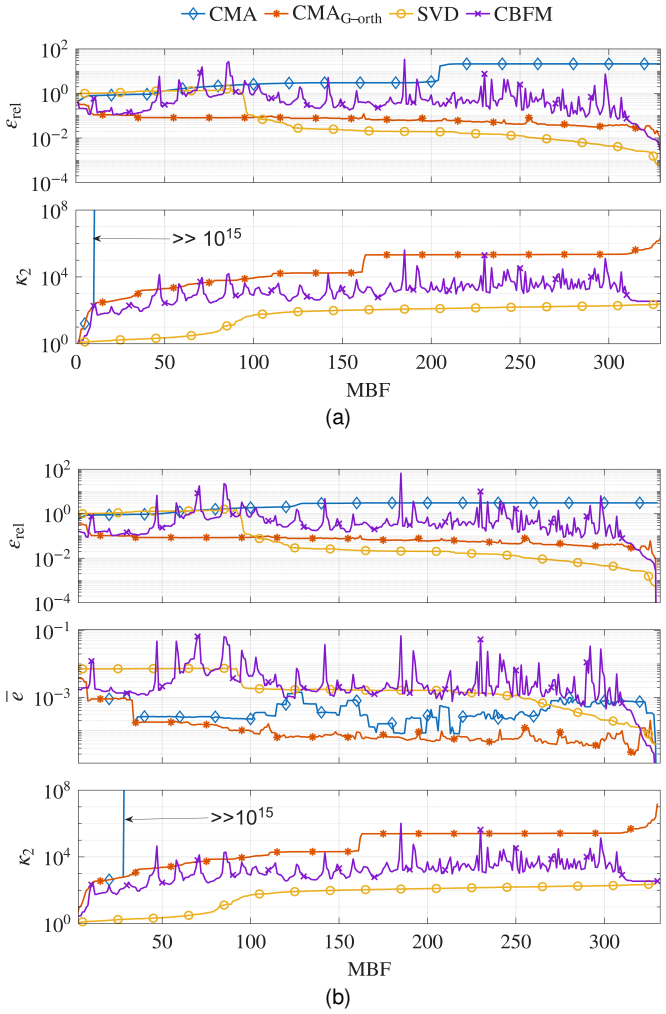


Fig. 3. Comparison of CMA, CMA$_{\text{G-orth}}$, CBFM, and SVD as functions of the number of retained MBFs. (a) Single-element results: relative current reconstruction error and condition number. (b) 8×8 array results: relative current reconstruction error, peak-normalized mean far-field error, and condition number.

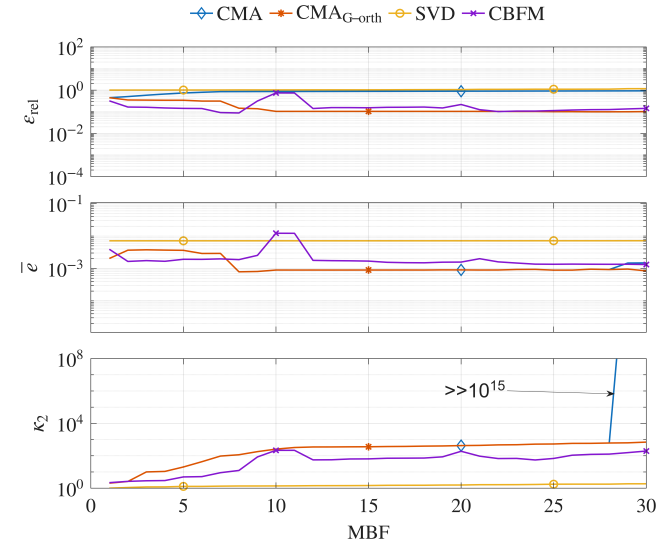


Fig. 4. Zoomed 8×8 array comparison of CMA, CMA$_{\text{G-orth}}$, CBFM, and SVD for 0–100 retained MBFs, showing current error, peak-normalized mean far-field error, and condition number.

results additionally include the peak-normalized mean far-field error. Figure 4 shows a zoomed view of the array results in the practically relevant low-rank range. In all plots, the horizontal axis denotes the number of retained MBFs per element. For the identical-element 8×8 array, this corresponds to $K = 64 \times$ (retained MBFs per element).

For the single-element case, CBFM offers the best accuracy at very low basis sizes, but its error curves are nonmonotonic as additional basis functions are retained. This does not contradict the SVD truncation, since the plotted quantity is the reduced MoM solution error rather than the response-space projection error. Additional retained functions may also affect conditioning and excitation coupling. CMA without explicit G-orthogonalization shows rapidly deteriorating conditioning once 11 MBFs are kept, which is mirrored by poorer current reconstruction than for $\text{CMA}_{\text{G-orth}}$. The SVD-based basis is least competitive at very small ranks, but remains the most stable construction as the basis size grows.

The identical-element 8×8 benchmark exhibits the same qualitative ordering, with condition-number trends and current-reconstruction errors largely following the single-element behavior. This is consistent with the decomposition in Section II: when the scaled coupling contribution $\mathbf{D}^{-1}\mathbf{C}$ is moderate, the array-level conditioning remains strongly influenced by the local block conditioning $\kappa_2(\mathbf{D})$. The main exception is the nonorthogonalized CMA basis, whose instability is delayed to larger basis sizes, with rapid condition-number growth starting once 29 MBFs are retained. CBFM again provides attractive low-rank compression but remains nonmonotonic as the basis is enriched. By contrast, the far-field error is less sensitive than the current error to the number of retained MBFs, since the radiation operator does not weight all current-error components equally.

Table II summarizes the minimum number of retained MBFs per element and the corresponding reduced dimension K required to reach an array-level far-field error below 10^{-3}. It directly quantifies the reduction from the full-order dimension of 21120 unknowns to the reduced dimension required by each MBF construction. The table highlights the practical low-rank tradeoff: CBFM requires more retained MBFs than CMA in this benchmark, whereas SVD requires the largest basis size but yields a well-conditioned reduced system.

Each element aperture supports 330 RWG basis functions. For visual clarity, the results are shown only up to 329 retained MBFs per element, since the full-order case at 330 MBFs is excluded for all methods. At this point, the far-field error reaches the numerical floor and causes clipping in the plots.

IV. Conclusion

This letter has presented a controlled benchmark comparison of CMA-, CBFM-, and SVD-based MBF constructions within a common reduced-order framework for cavity-backed reflectarray analysis. Since all methods were evaluated using the same formulation, discretization, partitioning, and solver settings, the observed differences can be attributed primarily to the MBF construction.

For the considered benchmark, CBFM achieves high accuracy with relatively few MBFs, but exhibits nonmonotonic

solution-error behavior as the basis is enriched. Explicit G-orthogonalization substantially improves both the conditioning and current-reconstruction accuracy of the CMA basis. The SVD-based basis produces the best-conditioned reduced systems, but requires more MBFs to reach the prescribed far-field accuracy.

The array results follow the main single-element current-reconstruction and condition-number trends, indicating that single-element analyses can serve as useful screening tools, although they are not substitutes for array-level validation. Overall, the results highlight the tradeoff between compression efficiency, numerical stability, and far-field accuracy in MBF-based reflectarray analysis. Future work will address heterogeneous arrays and reduced-order efficiency.

ACKNOWLEDGMENT

This work was funded by the European Union, under ANTERRA 101072363 HORIZON-MSCA-2021-DN-01. Views and opinions expressed are however those of the author(s) only and do not necessarily reflect those of the European Union. Neither the European Union nor the granting authority can be held responsible for them.

The first author gratefully acknowledges the memory of his mother for her constant support and encouragement.

REFERENCES

[1] K. Sewraj and M. M. Botha, "Overview of macro basis function research for antenna array solvers," in *2022 4th International Conference on Emerging Trends in Electrical, Electronic and Communications Engineering (ELECOM)*, 2022, pp. 1–5.

[2] C. Craeye, J. Laviada, R. Maaskant, and R. Mittra, "Macro basis function framework for solving Maxwell's equations in surface-integral-equation form," *Forum for Electromagnetic Research Methods and Application Technologies (FERMAT)*, vol. 3, pp. 1–16, 2014.

[3] D. Lin, L. Manholm, and R. Maaskant, "Fast MoM-based solvers for cavity-backed reflectarrays and RIS design," in *Proceedings of the 2026 European Conference on Antennas and Propagation (EuCAP)*, 2026, accepted.

[4] D. Lin, P. Aghdam, and R. Maaskant, "Modeling of conformal reflectarrays through domain decomposition using a generalized admittance approach," in *2025 Asia-Pacific Microwave Conference (APMC)*, 2025, pp. 1–3.

[5] D. Lin, L. Manholm, O. Talcoth, S. Agneessens, P. Aghdam, and R. Maaskant, "Fast scattering analysis of large open-cavity based reflectarrays using a hybrid method of moment and physical optics approach," in *2025 International Conference on Electromagnetics in Advanced Applications (ICEAA)*, 2025, pp. 0682–0686.

[6] R. Maaskant *et al.*, "Domain decomposition analysis of open-cavity-based array elements - roadmap toward analyzing large-scale reflectarrays and reconfigurable intelligent surfaces," in *2025 International Conference on Electromagnetics in Advanced Applications (ICEAA)*, 2025, pp. 687–692.

[7] D. Lin, L. Manholm, O. Talcoth, P. Aghdam, and R. Maaskant, "Hybrid domain-decomposition/physical-optics analysis of finite reconfigurable reflectarrays using characteristic-mode macro basis functions," Manuscript submitted for publication, submitted to IEEE Antennas and Wireless Propagation Letters (AWPL).

[8] X. Deng, D. Zhang, Y. Chen, and S. Yang, "Characteristic mode analysis: Application to electromagnetic radiation, scattering, and coupling problems," *Chinese Journal of Electronics*, vol. 32, no. 4, pp. 663–677, 2023.

[9] J. F. Gao and F. H. Lin, "Modeling and Analysis of Wideband Multilayer Metasurface Antenna Array Using Characteristic-Mode Analysis," *IEEE Trans. Antennas Propag.*, vol. 71, no. 3, pp. 2832–2836, 3 2023.

[10] R. Harrington and J. Mautz, "Theory of characteristic modes for conducting bodies," *IEEE Trans. Antennas Propag.*, vol. 19, no. 5, pp. 622–628, 1971.

[11] M. Zhang, C. Jia, Z. He, Z. Li, and D. Ding, "A fast analysis method based on characteristic mode method for large scale array structure," in *2022 IEEE 10th Asia-Pacific Conference on Antennas and Propagation (APCAP)*, 2022, pp. 1–2.

[12] R. Harrington and J. Mautz, "Characteristic modes for aperture problems," *IEEE Trans. Microw. Theory Tech.*, vol. 33, no. 6, pp. 500–505, 1985.

[13] E. Erçil, L. Alatan, and A. Civi, "An efficient numerical solution method for reflectarrays of varying element sizes," *IEEE Trans. Antennas Propag.*, vol. 63, no. 12, pp. 5668–5676, 2015.

[14] C.-S. Park, Y.-R. Jeong, I.-P. Hong, and J.-G. Yook, "Block size optimization of CBFM for scattering problems," *IEEE Trans. Antennas Propag.*, vol. 66, no. 10, pp. 5370–5377, 2018.

[15] K. Konno, Q. Chen, K. Sawaya, and T. Sezai, "Optimization of block size for CBFM in MoM," *IEEE Trans. Antennas Propag.*, vol. 60, no. 10, pp. 4719–4724, 2012.

[16] R. Maaskant, C. Bencivenni, and M. V. Ivashina, "Characteristic basis function analysis of large aperture-fed antenna arrays," in *8th European Conference on Antennas and Propagation, EuCAP 2014*. Institute of Electrical and Electronics Engineers Inc., 2014, pp. 2427–2431.

[17] R. Maaskant, R. Mittra, and A. Tijhuis, "Fast analysis of large antenna arrays using the characteristic basis function method and the adaptive cross approximation algorithm," *IEEE Trans. Antennas Propag.*, vol. 56, no. 11, pp. 3440–3451, 2008.

[18] E. Lucente, A. Monorchio, and R. Mittra, "An iteration-free MoM approach based on excitation independent characteristic basis functions for solving large multiscale electromagnetic scattering problems," *IEEE Trans. Antennas Propag.*, vol. 56, no. 4, pp. 999–1007, 2008.

[19] P. Du, W. Xiang, and S.-S. Zhu, "A comparison of MB-CBFM and modified ASED basis function method to analyze interconnected finite periodic arrays," *IEEE Antennas Wireless Propag. Lett.*, vol. 21, no. 9, pp. 1822–1826, 2022.

[20] T. Tanaka, K. Niino, and N. Nishimura, "Characteristic basis function method combined with Krylov-Calderón preconditioner for PMCHWT formulation," *IEEE Trans. Antennas Propag.*, vol. 72, no. 3, pp. 2578–2591, 2024.

[21] H. Shao, K. Fu, Z. Fu, X. Ying, and J. Hu, "A fast model order reduction method for electromagnetic scattering of large periodic arrays with connected elements," *IEEE Trans. Antennas Propag.*, vol. 71, no. 11, pp. 9142–9147, 2023.

[22] T. Marinović and R. Mittra, "Characteristic basis function method using single high-level basis function per subdomain for efficient analysis of large periodic array antennas," in *2023 IEEE International Symposium on Antennas and Propagation and USNC-URSI Radio Science Meeting (USNC-URSI)*. IEEE, 7 2023, pp. 807–808.

[23] J. Helander, D. Tayli, and D. Sjöberg, "A comparison of macro basis function methods for interconnected endfire antenna arrays," *IEEE Antennas Wireless Propag. Lett.*, vol. 16, pp. 2159–2162, 2017.

[24] K. Sewraj and M. M. Botha, "Fast analysis of large antenna arrays with static and dynamic macro basis function methods," in *2024 International Conference on Electromagnetics in Advanced Applications (ICEAA)*, 2024, pp. 273–275.

[25] I. Zhabitskiy and M. M. Botha, "Array antenna solver based on macro basis functions, with improved accuracy," in *2022 International Conference on Electromagnetics in Advanced Applications (ICEAA)*, 2022, pp. 329–331.

[26] C. Craeye, "A fast impedance and pattern computation scheme for finite antenna arrays," *IEEE Trans. Antennas Propag.*, vol. 54, no. 10, pp. 3030–3034, 2006.

[27] R. Harrington and J. Mautz, "A generalized network formulation for aperture problems," *IEEE Trans. Antennas Propag.*, vol. 24, no. 6, pp. 870–873, 11 1976.

[28] A. Booysen, "Aperture theory and the equivalence theorem," in *IEEE Antennas and Propagation Society International Symposium. 1999 Digest. Held in conjunction with: USNC/URSI National Radio Science Meeting (Cat. No.99CH37010)*, vol. 2. IEEE, 1999, pp. 1258–1261.

[29] S. Rao, D. Wilton, and A. Glisson, "Electromagnetic scattering by surfaces of arbitrary shape," *IEEE Trans. Antennas Propag.*, vol. 30, no. 3, pp. 409–418, 5 1982.

[30] L. N. Trefethen and I. David Bau, *Numerical Linear Algebra*. SIAM, 1997.

[31] N. J. Higham, *Accuracy and Stability of Numerical Algorithms*, 2nd ed. SIAM, 2002.

[32] P.-S. Kildal, *Foundations of Antenna Engineering: A Unified Approach for Line-of-Sight and Multipath*. Gothenburg, Sweden: Kildal Antenn AB, Updated March 15, 2021.